

A submicron Si@C core-shell intertwined with carbon nanowires and graphene nanosheet as a high-performance anode material for lithium ion battery



Zhengqing Fan^{a,\$}, Yiting Wang^{a,\$}, Songsheng Zheng^{a,*}, Ke Xu^b, Jianyang Wu^{b,*}, Si Chen^a, Junhua Liang^a, Aodi Shi^a, Zhaolin Wang^{a,*}

^a College of Energy, Xiamen University, Xiamen 361102, PR China

^b College of Physical Science and Technology, Xiamen University, Xiamen 361005, PR China

ARTICLE INFO

Keywords:

Submicron Si@C-Ni
Core-shell structure
Carbonization
Anode for lithium ion battery

ABSTRACT

Silicon is widely used as anode for lithium-ion batteries (LIBs). However, its application is limited due to some problems such as large volume expansion. In this work, silicon waste from wafer slicing via diamond wire saw technology in photovoltaic industry is used as raw materials. A submicron core-shell structure Si@C intertwined with CNWs and graphene nanosheet, is prepared as anode for LIBs by hydrothermal process. The anode retains a specific capacity of 2514.8 mAh g⁻¹ with capacity retention of 75.8% after 360 cycles under a current of 0.1 C and 1548.9 mAh g⁻¹ after 1000 cycles under 0.2 C. In addition, it maintains 1596.9 mAh g⁻¹ (1.0 C), 925.3 mAh g⁻¹ (2.0 C) after several rate testing of 0.1 C to 2.0 C. A COMSOL Multiphysics and MD simulation are performed to examine the lithiation-induced volume expansion of silicon. The results demonstrate that, the lamellar micron silicon can achieve a stable lithium intercalating capacity larger than 2100 mAh g⁻¹, which agrees well with our experimental results. It is demonstrated that the submicron Si from the kerf waste in the photovoltaic slicing process via diamond wire saw technology are available as direct raw materials for high performance anode of LIBs.

1. Introduction

With the rapid development of modern technology, such as modern communication, electric vehicles, artificial intelligence, and etc., lithium-ion batteries (LIBs) are widely used in energy storage due to its high capacity, high security, rechargeability and light weight [1,2]. In contrast to the commercial graphite anodes of LIBs, who had a limited theoretical capacity of 372 mAh g⁻¹ [3], silicon could better meet the energy density demands because of its super high theoretical capacity (4200 mAh g⁻¹) and relatively low delithiation potential (~0.4 V vs. Li⁺/Li) [4–6]. Moreover, a higher voltage platform of silicon would provide a safety guarantee for LIBs. Therefore, silicon has become attractive as an ideal anode candidate for modern LIBs [7–10].

Unfortunately, as a semiconductor element, Si has poor electrical conductivity. During lithiation/delithiation of LIBs, a large volume expansion (~300%) in Si anode will occur, even worse, the repeated generation and destruction of the surface solid electrolyte interphase (SEI) film will promote the formation and growth of the lithium dendrites

[11–13]. All these drawbacks will cause low electrical performance, pulverization of Si anode and rapid capacity fading of LIBs [11,14,15].

Therefore, a large quantity of efforts have been made to improve the performance of silicon-based anode for LIBs, such as nano-scale Si composites [16], constructing Si-based alloys [17,18], fabricating appropriate architectures like designing hollow or porous Si materials [19,20] and so on. Among these solutions, minimizing the size of silicon is beneficial to reduce the electrode pulverization from expansion of volume and bridge the transfer distance of Li-ion, leading to increasing reversible capacity and cycle life. However, the surface of the Si nano-sized structure is directly exposed to electrolyte and damaged by undergoing repeated destruction and re-generation of SEI film, which results in decreasing the electrical performance [21,22].

Additionally, the nano-Si process is costly and complex, which offers an opportunity to make good use of submicron silicon to cut down expenses [23]. To guarantee Si anode with better protection and higher electrical performance, carbon materials like graphite, graphene and carbon nanotube have been widely applied to improve the conductivity and confine volume expansion of Si anode [24–28]. Core-shell structure

* Corresponding authors.

E-mail addresses: songsheng@xmu.edu.cn (S. Zheng), jianyang@xmu.edu.cn (J. Wu), forestwang@xmu.edu.cn (Z. Wang).

\$ contribute equal to this article

Si@C material shows high capacity and relatively stable cycling performance, but the repeated volume change and weak bonds between carbon shells and silicon cores often cause carbon shells easily detached from joint and electrolyte directly contacted with silicon, which leads to the sharp capacity fading in batteries [29]. To avoid the above problems, it is significant to enhance the electrical conductivity by converting disorder carbon to graphene.

On the other hand, silicon is the main material in the commercial photovoltaic production, and there is more than 30% of silicon being wasted in the wafer slicing process by diamond wire sawing (DWS) [30,31]. With the prosperity of photovoltaic industry, the silicon wafer's demand will increase rapidly. Therefore, it is urgent to recycle the silicon kerf waste from the slicing slurry. Recently, many researchers have concentrated on the reuse of waste silicon for LIBs, and have achieved certain good results [32–36]. However, further investigations on the recycling of waste silicon for LIBs are still necessary to make it commercially available.

In our previous work, core-shell structure Si@C materials have been successfully prepared by using the submicron silicon from kerf waste, and high electrochemical performance has been achieved. However, due to the low degree of graphitization of the prepared carbon shell, graphene needs to be added to improve the rate performance of the sample [37]. In this article, silicon waste from slicing wafers in photovoltaic industry was used as raw materials, glucose was added as carbon sources and nickel acetate tetrahydrate was introduced as a catalyst to improve graphitization. A grid with carbon nanowires (CNWs) is woven around the Si@C balls to increase the network electrical conductivity, thereby the stability of the electrochemical performance of the anodes is improved. As a result, the as prepared Si@C-Ni anode materials are of high capacity of $3317.6 \text{ mAh g}^{-1}$ with an initial coulombic efficiency of 76.76% and still retains a specific capacity of $2514.8 \text{ mAh g}^{-1}$ with capacity retention of 75.8% after 360 cycles under a current of 0.1 C; and retains a specific capacity of $1548.9 \text{ mAh g}^{-1}$ after 1000 cycles under a current of 0.2 C. Besides, it maintains $1596.9 \text{ mAh g}^{-1}$ (1.0 C), 925.3 mAh g^{-1} (2.0 C) after several rate testing of 0.1 C to 2.0 C, and is stable at $\sim 3000 \text{ mAh g}^{-1}$ when the current returns to 0.1 C. These suggest the samples we made are superiorly high-performance anode materials for LIBs.

2. Experimental

2.1. Preparation composites

The silicon waste block obtained by pressure filtration from the diamond wire slicing process of silicon wafer was used as raw material. Firstly, a core-shell structure Si@C material was synthesized. As described in our previous work [37], briefly, the silicon block was ground and added into a stainless-steel autoclave together with glucose and distilled water, and then stirring to uniformity. Then, the autoclave was heated at 190°C for 12 h. After that, the resulting solid was filtrated, dried at 80°C for 12 h, and calcinated at 800°C for 12 h to form the core-shell structure Si@C materials. Subsequently, the as prepared Si@C sample and the nickel acetate tetrahydrate agent were dispersed in ethanol solution, and stirring was applied for 12 h. Then, the mixture was dried at 80°C , and carbonized at 950°C , and then cooled to room temperature. The sample obtained was named as Si@C-Ni. The microstructure evolution process is sketched in Fig. 1. The different colored spheres represent the shell made up of a carbon skeleton, where the pink and blue spheres are the carbon and oxygen atoms that make up the carbon skeleton and the yellow spheres represent the loaded nickel catalyst.

2.2. Properties characterization

The morphologies, surface structures and elemental analysis were carried out using field-emission scanning electron microscopy (FESEM, Zeiss SUPRA 55) with energy dispersive spectrometer (EDS). The clarify

microstructure of Si@C and Si@C-Ni composites were obtained by TEM (JEM-2100). The crystal structures were studied by X-ray diffraction (XRD) on the Rigaku Ultima IV diffractometer using Cu K α radiation at 40 kV and 30 mA at a scan rate of 5° min^{-1} . Raman spectroscopy was analyzed on the IHR-320 spectrometer with an Ar ion radiation laser beam (excitation wavelength is 638 nm) and an incident power of 1 mW .

2.3. Electrochemical measurements

The electrochemical performances of Si@C-Ni were demonstrated with CR2032 coin half cell batteries [37] and tested on LAND-CT2001A Battery System (Wuhan Btrbts Technology Co. Ltd., China) at 25°C under galvanostatic charge/discharge between 0.01 V and 1.2 V with a 0.05 C rate for the first 2 cycles, and separately at the rate of 0.1 C and 0.2 C for the next hundreds of cycles. The rate capability was tested at charge/discharge rates of 0.05 C for the first two cycles, and at 0.1 C , 0.2 C , 0.4 C , 0.6 C , 0.8 C , 1.0 C , 2.0 C for 10 cycles each, finally back to 0.1 C for 10 cycles. Electrochemical impedance spectral (EIS) was tested in a frequency range between 0.01 Hz and 100 kHz at an amplitude of 0.005 V .

3. Results and discussion

The SEM morphologies of the Si@C and Si@C-Ni were shown in Fig. 2.

As can be seen from Fig. 2a, b and c, the as prepared core-shell structure Si@C balls are uniform with size of submicron level (around 700–1000 nm). An excessive amount of glucose results in a small amount of floccles surrounding the ball, which is disordered carbon [37]. When comparing to Fig. 2d, e and f, carbon nanowires (CNWs) can be observed. These carbon nanowires are wrapped around the core-shell structure Si@C balls, forming a network structure. Furthermore, it can be found from Fig. 2h that the Ni nanoparticles are evenly distributed in the Si@C-Ni samples. To further determination, the HRTEM analysis are shown in Fig. 3 and Fig. 4.

As is clearly shown from Fig. 3a to Fig. 3c, the submicron Si@C balls was connected to each other by the carbonaceous materials. The diffraction pattern in Fig. 3d doesn't give valuable message, as well as the 800 kX image (Fig. 3e) doesn't have lattice fringes, which indicate that the carbon shell has not been well crystallized. On the other hand, the carbonaceous materials surrounding the Si@C ball are shown in Fig. 3f to Fig. 3h, which looks like a carbon sheet. The bright diffraction pattern in Fig. 3i proves that the graphitization degree is very high, and the obvious disordered lattice fringes in Fig. 3j supports the graphitization result, where the fringes distances are 0.29 nm , 0.33 nm and 0.36 nm , corresponding to the crystal planes of (100), (002) and (001), respectively. The discrepancies of fringe distances further indicate the disordered state of graphitization.

On the contrary, after catalyzed by Ni, things are getting changed, as is shown in Fig. 4. As is shown in Fig. 4a–c, the Si@C balls are not changed obviously, although the 800 kX image in Fig. 4e doesn't show clear lattice fringes on the ball surface, but several fuzzy diffractive rings can be observed in the diffraction pattern (in Fig. 4d), which relates to the crystal plane of (104), (114), (101) and (103). It means that the crystallization on the ball surface are getting better via the catalysis of nickel. From Fig. 4f–j, it can be clearly seen that the CNWs are formed. The bright diffraction pattern in Fig. 4h proves a high quality of CNWs, as well as the obvious ordered lattice fringes in Fig. 4j supports the result, where the fringe distances are 0.36 nm , corresponding to the crystal planes of (001).

Moreover, as is shown in Fig. 4k–o, the carbonaceous surrounding the Si@C ball have been converted to graphene nanosheet. The obvious ordered lattice fringes in Fig. 4o support the graphitization result, where the fringe distances are uniform as 0.36 nm , corresponding to the crystal planes of (001).

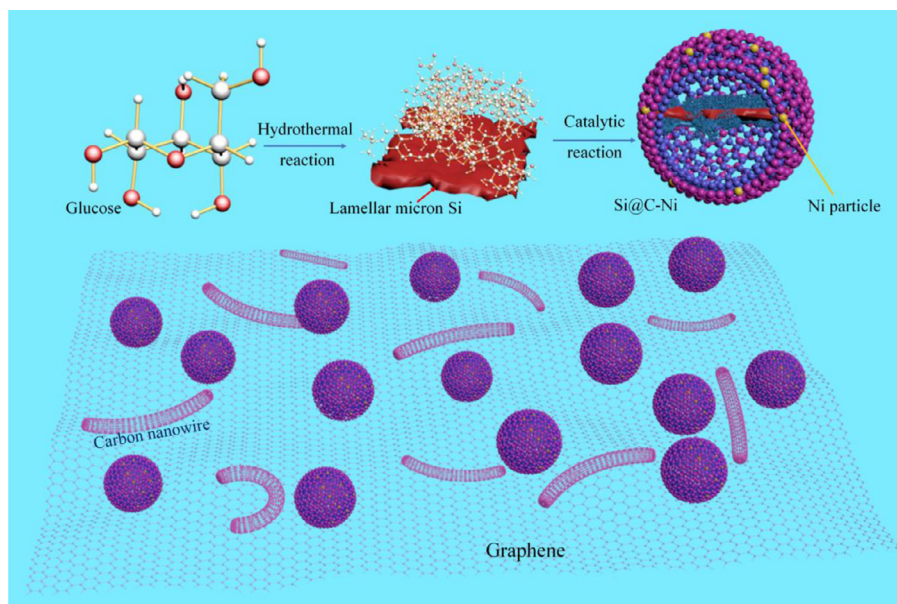


Fig. 1. The microstructure evolution process of $\text{Si}@\text{C-Ni}$ composites.

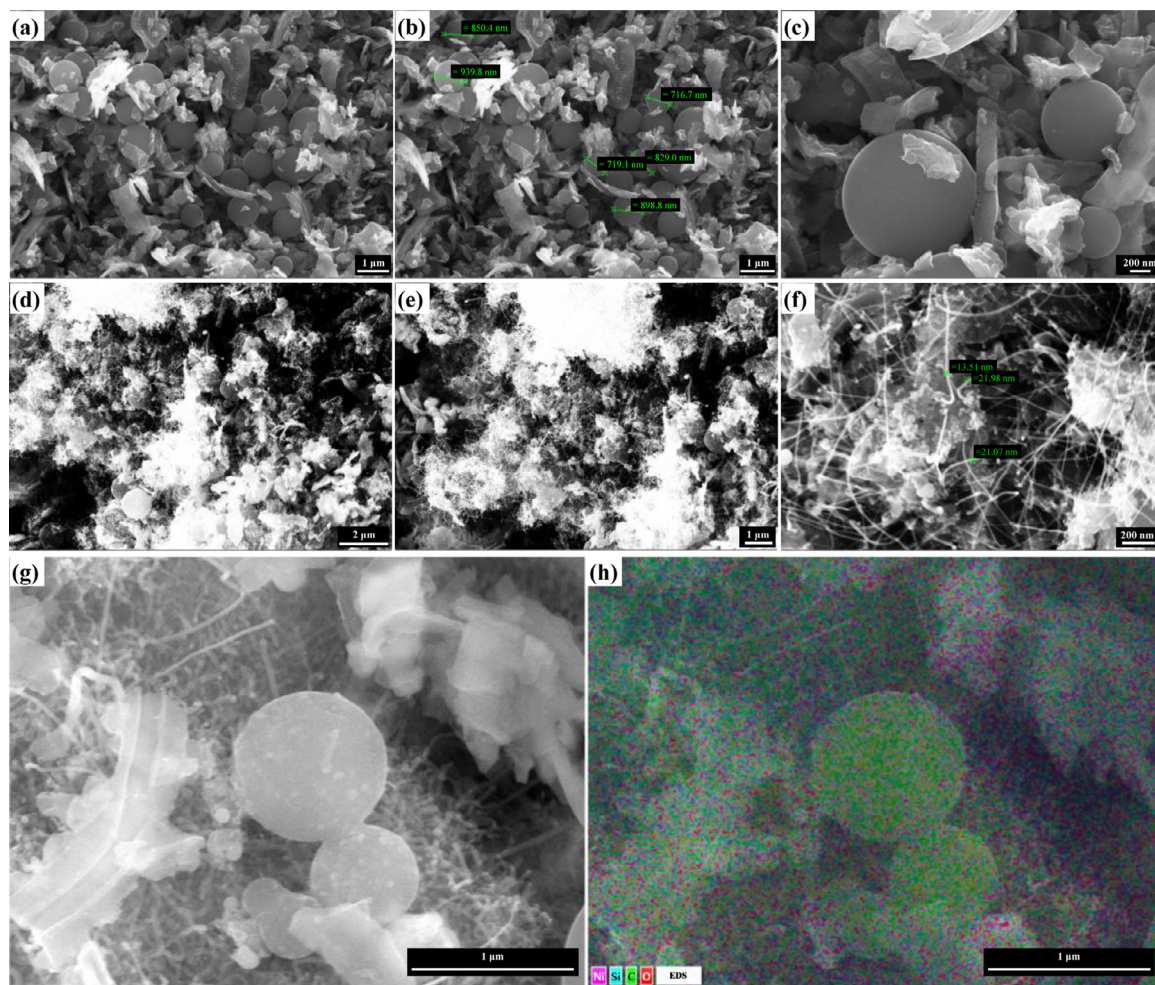


Fig. 2. SEM images of $\text{Si}@\text{C}$ composites: (a) and (b) 10kX, (c) 30kX; and $\text{Si}@\text{C-Ni}$ samples: (d) 7.19kX, (e) 8.15kX, (f) 50.27kX, (g) electronic image for EDS analysis, and (h) EDS elemental distribution map.

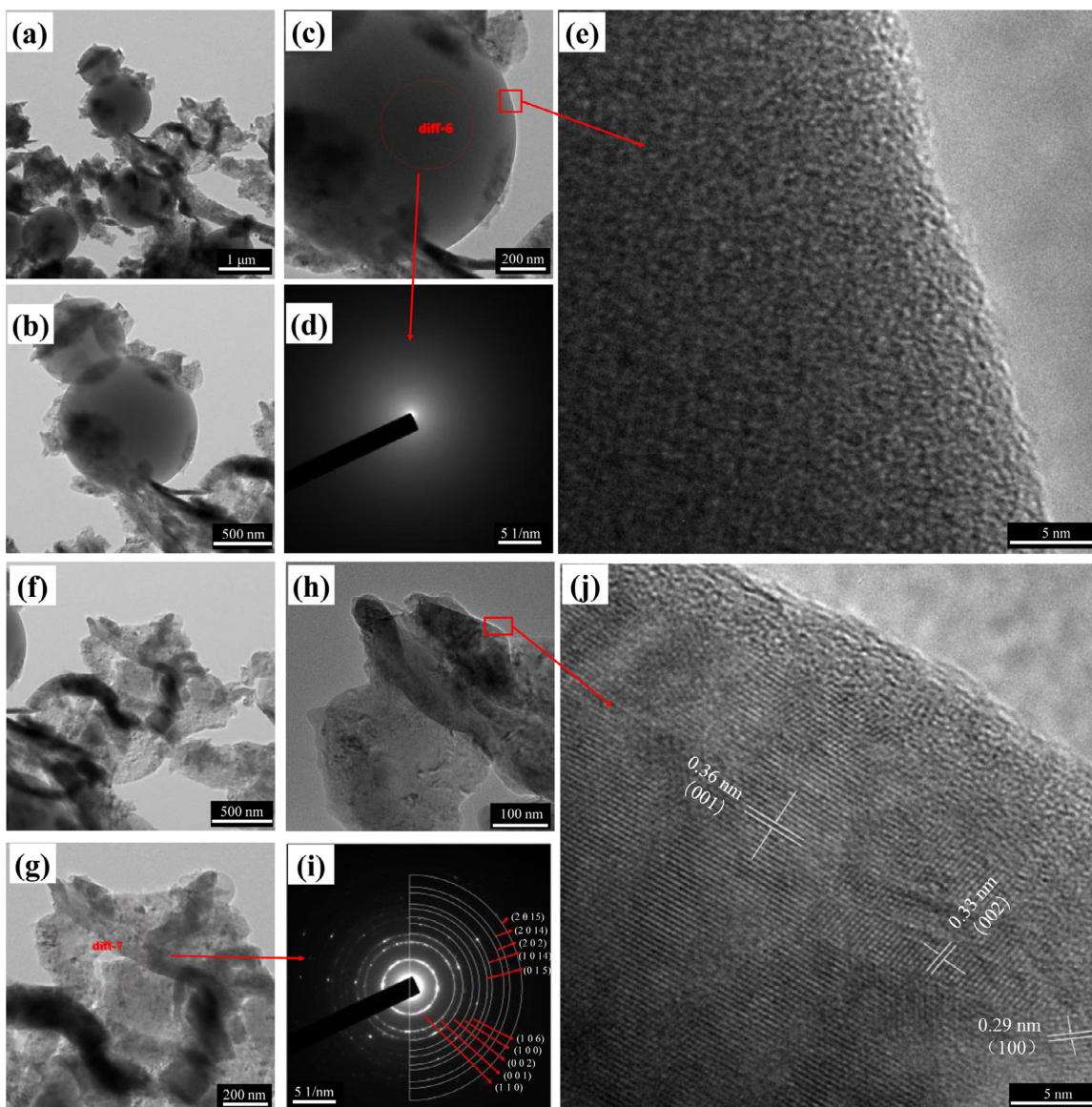


Fig. 3. The HRTEM images of Si@C ball: (a) 5kX, (b) 10kX, (c) 20kX, (d) diffraction pattern, (e) 800kX; and the HRTEM images of carbonaceous: (f) 10kX, (g) 20kX, (h) 50kX, (i) diffraction pattern, and (j) 800kX.

The structure of Si@C and Si@C-Ni composites were further explored by the X-ray diffraction (XRD) and Raman spectroscopy, and shown in Fig. 5.

As shown in Fig. 5a, there are only diffraction peaks of Si in the XRD patterns of the Si@C samples, which confirms that the carbon in the Si@C samples is in disorder. As a comparison, SiC and C peaks are observed in the XRD patterns of Si@C-Ni samples, except for the peaks of Si, Ni and Ni₂Si phases. On the other hand, in the Raman spectrum of Si@C composites (in Fig. 5b), the peaks at 303 cm⁻¹, 512 cm⁻¹ and 945 cm⁻¹ relate to Si crystal, D-peak at 1332 cm⁻¹ and G-peak at 1590 cm⁻¹ represent amorphous carbon and graphitized carbon, respectively [38]. The relative peak intensity ratio (I_D/I_G) of peak D and peak G can represent the degree of graphitization of carbon materials to a certain extent. The smaller the I_D/I_G ratio, the higher the degree of graphitization of carbon materials [39]. The I_D/I_G ratio of Si@C samples is 1.147, also indicating a low carbonization on the Si@C samples. In contrast, the I_D/I_G ratio of the Si@C-Ni composites are 1.029, which means a higher graphitization of carbon. Moreover, the Raman spectrum of the Si@C-Ni composites show a typical 2D peak of graphene (or graphite) at 2645 cm⁻¹ [40,41].

The above results demonstrate that the disordered carbon in the Si@C-Ni samples are catalyzed by Ni to form CNWs and graphene nanosheet, so that the overall graphitization of the materials is significantly improved. In terms of mechanism, nickel is widely acknowledged as a high-efficient catalyst for graphitization of carbon [42–44]. Solid carbon sources can gradually dissolve in nickel even at low annealing temperature. With the temperature increasing, more and more dissolved carbons diffuse to the surface and recrystallize to form graphene layer coating on the nickel layer [45,46]. The formation mechanism of carbon nanowires is similar to the graphitization of disordered carbon. CNWs are generated by disordered carbon with single nickel nanoparticles as attachment points in a directed manner. Therefore, in this work, the nickel in Si@C-Ni assists in forming a network with CNWs and graphene nanosheet intertwined with the Si@C ball.

In order to evaluate the electrochemical performance of Si@C and Si@C-Ni composites as anode electrodes of coin cells with Li as counter electrode, cycle performance, rate performance and electrochemical impedance spectral (EIS) were tested. The results are shown in Fig. 6.

As is shown in Fig. 6a, compared to Si@C electrode, the cycle performance of the Si@C-Ni electrode has been greatly improved. The ini-

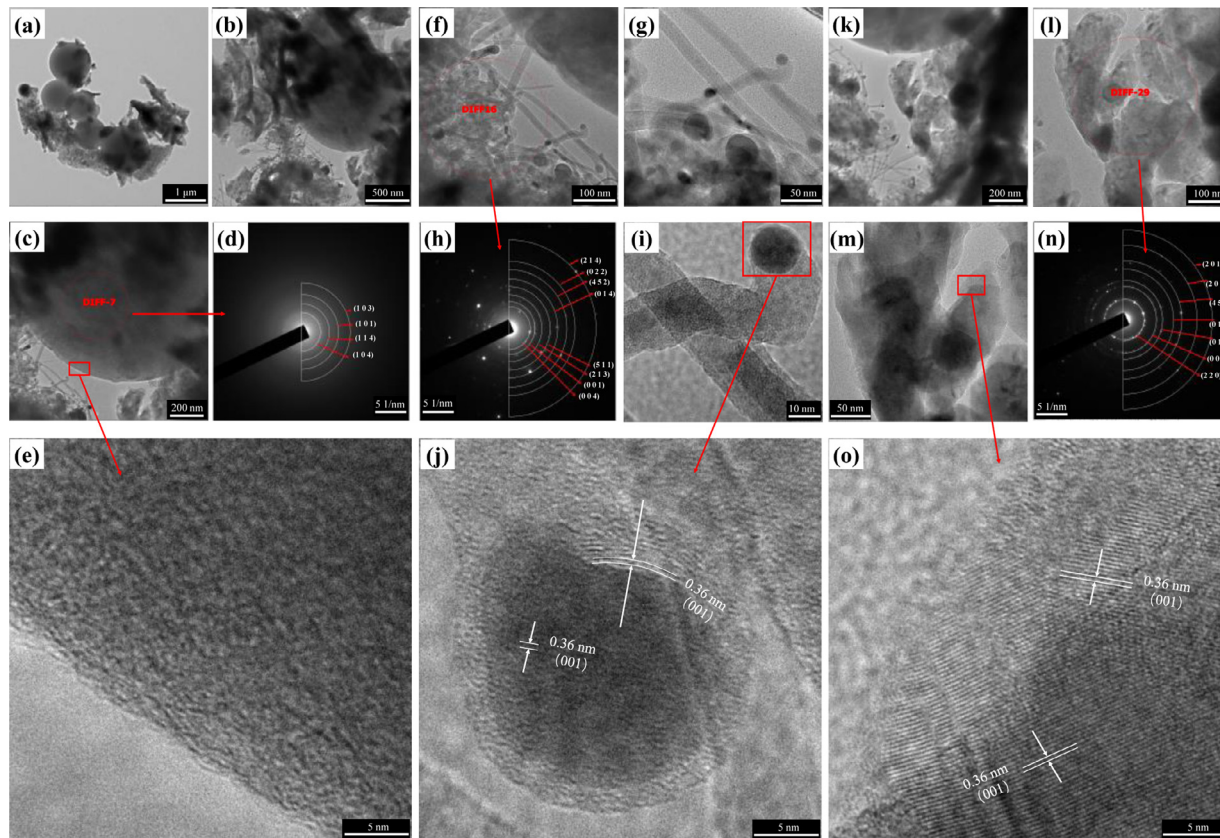


Fig. 4. The HRTEM images of Si@C-Ni samples: (a) 5kX, (b) 10kX, (c) 20kX, (d) diffraction pattern, (e) 800kX; and the HRTEM images of CNWs: (f) 50kX, (g) 400kX, (h) diffraction pattern, (i) 400kX, (j) 800kX; and the HRTEM images of graphene nanosheet: (k) 20kX, (l) 50kX, (m) 100kX, (n) diffraction pattern, and (o) 800kX.

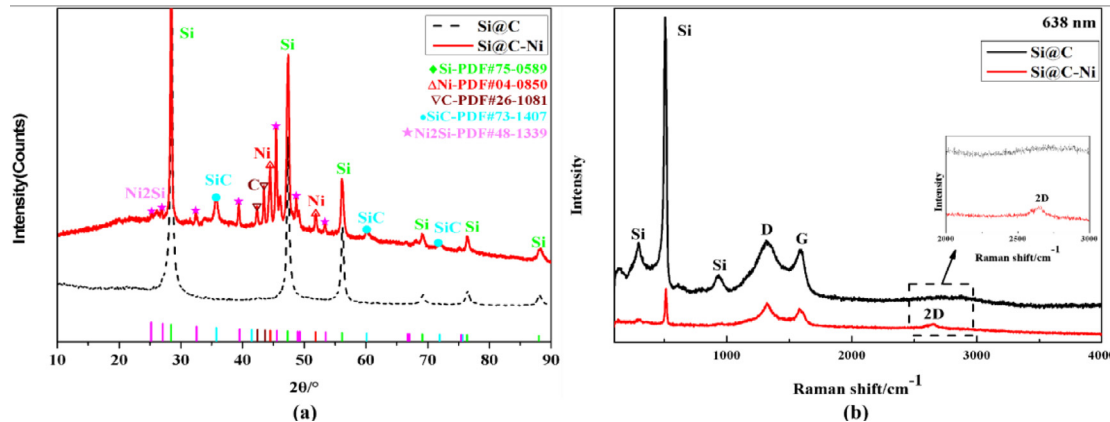


Fig. 5. Structure characterizations of Si@C and Si@C-Ni composites: (a) XRD patterns, (b) Raman spectra.

tial specific discharge capacity of Si@C-Ni electrode is 3317.6 mAh g⁻¹ with a coulombic efficiency of 76.76%. The electrode still retains a specific discharge capacity of 2514.8 mAh g⁻¹ with capacity retention of 75.8% after 360 cycles at a rate of 0.1 C (1 C = 4200 mA g⁻¹); and retains a specific discharge capacity of 1548.9 mAh g⁻¹ after 1000 cycles at a rate of 0.2 C. It indicates that the Si@C-Ni electrode exhibits extremely slow capacity decay. On the contrary, the Si@C electrode has a sharp decay in its cycles. In addition, as can be seen from Fig. 6a, the coulombic efficiency of the Si@C-Ni electrode during cycling is close to 100%, indicating a good reversibility during charging/discharging process.

Fig. 6b and c are the charge/discharge profiles of Si@C-Ni electrode at 0.1 C and 0.2 C in different cycles. It can be seen from the galvanostatic charge/discharge curves that the irreversible capacity loss of the first cycle is relatively large, which is due to the formation of the SEI film. There is a very long discharge platform between 0.15 and 0.01 V, which corresponds to the process of the alloying reaction between Si and Li to form Li_xSi alloy. The charging curves have a longer plateau at 0.3~0.5 V, which corresponds to the higher reversible specific capacity of the battery. Fig. 6d is the CV curves of Si@C-Ni electrode in the first 6 cycles, the reduction peak at about 0.83 V in the first cathodic scan corresponds to the formation of the SEI film, and this reduction peak

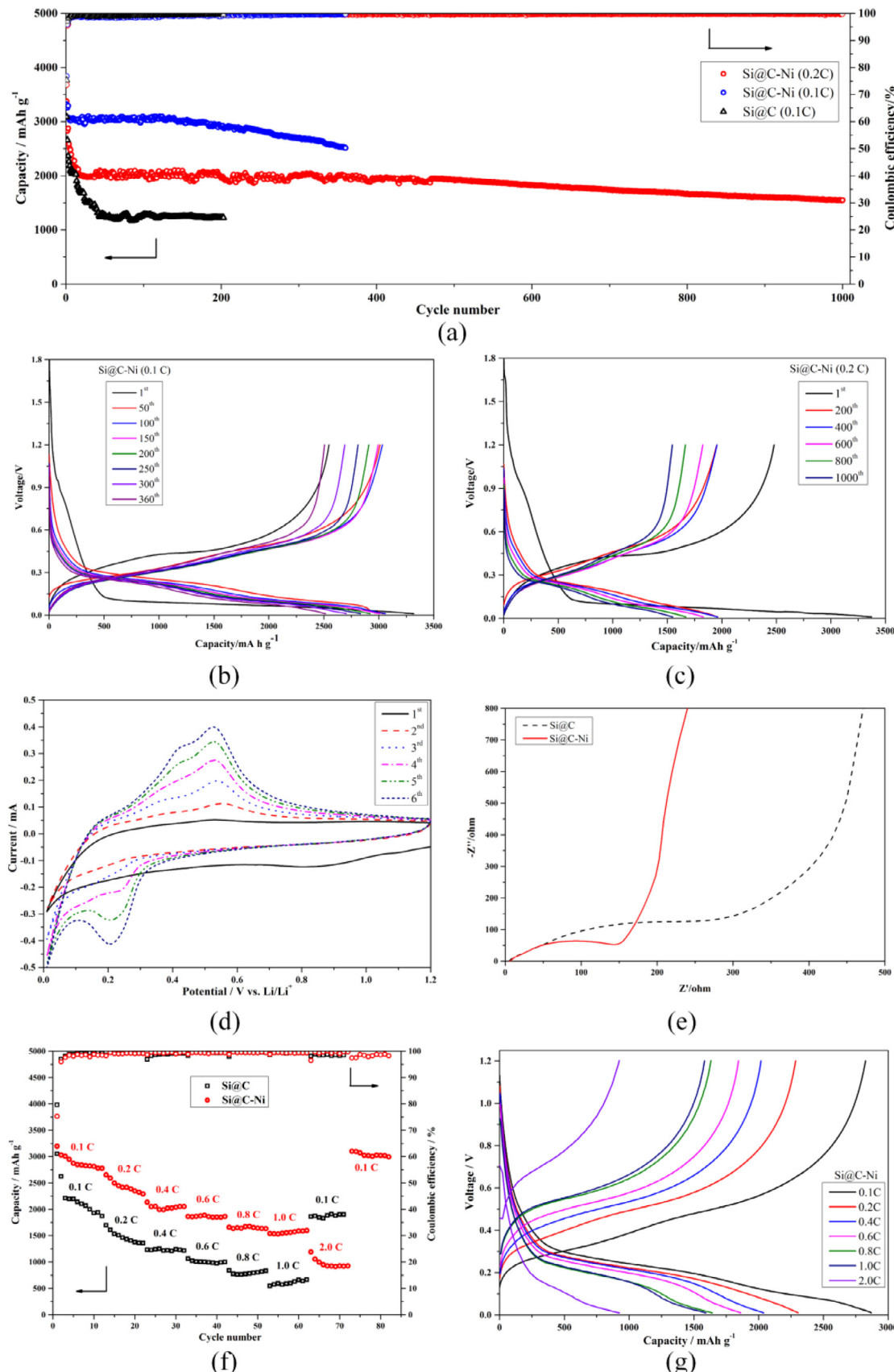


Fig. 6. Electrochemical performance of Si@C and Si@C-Ni: (a) galvanostatic charge/discharge performance of Si@C and Si@C-Ni electrodes, (b) and (c) charge/discharge profiles of galvanostatic charge, (d) current-voltage curves, (e) EIS curves, (f) rate capability, and (g) rate capability charge/discharge profiles of rate charge.

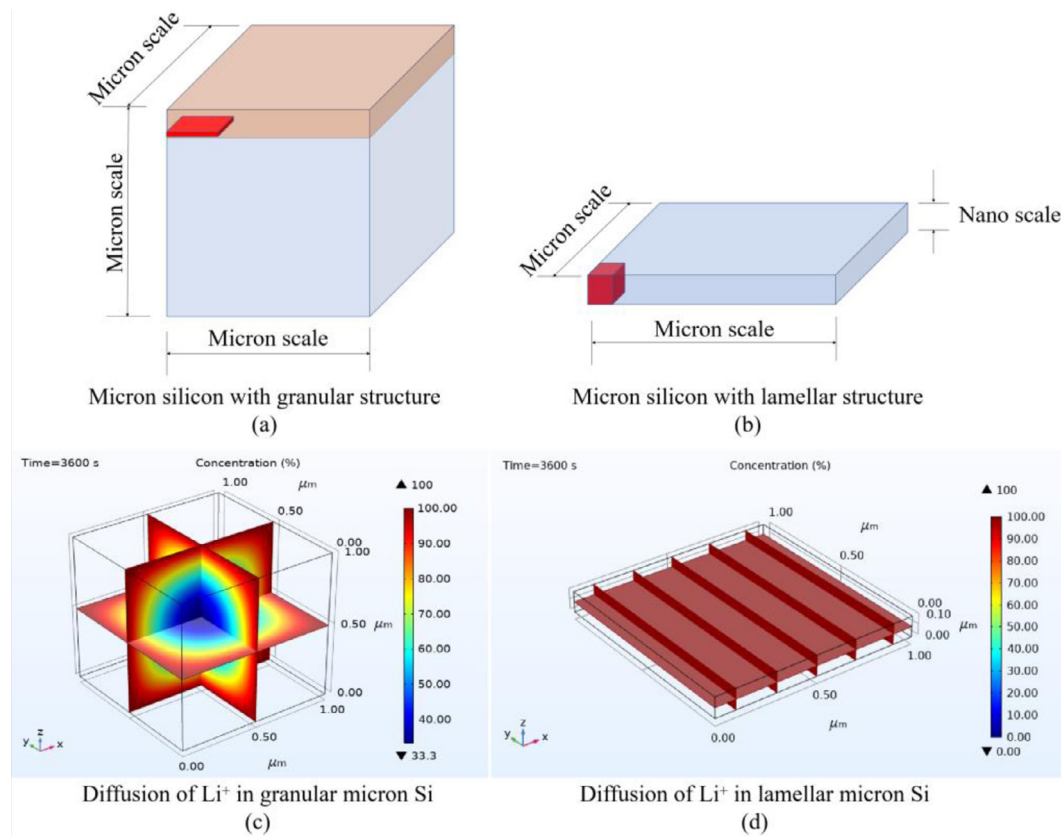


Fig. 7. Micron silicon structure: (a) granular structure, (b) Lamellar structure, and simulation of Li^+ diffusion by COMSOL Multiphysics in: (c) granular structure, (d) Lamellar structure.

no longer appears in the subsequent cycles. The reduction peak at 0.2 V corresponds to the formation of the Li_xSi alloy [47], and the oxidation peaks at 0.41 V and 0.52 V correspond to the delithiation process of the electrode. As the cycle progresses, the intensity of the reduction peak and the oxidation peak gradually increase, indicating improved electrode lithiation/delithiation kinetics [48].

Fig. 6f shows the attenuation of the reversible discharge capacity of two samples at different rates. Apparently, as the current rate increases, the discharge capacity of both electrodes will decrease. Whereas, at the same rate, the $\text{Si}@\text{C-Ni}$ electrode shows slower capacity decay. The $\text{Si}@\text{C-Ni}$ electrode maintains 2776.7, 2291.1, 2051.7, 1862.5, 1630.6, 1596.9, 925.3 mAh g⁻¹ at each rate of 0.1 C to 2.0 C, and when the current returns to 0.1 C, it recovers to about 3000 mAh g⁻¹. Furthermore, the EIS curves in Fig. 6e tested in a frequency range between 0.01 and 100 kHz at an amplitude of 0.005 V are used to study the resistance of electrode materials. The radius of corresponding semicircle of $\text{Si}@\text{C}$ is larger than that of $\text{Si}@\text{C-Ni}$, which suggests the $\text{Si}@\text{C-Ni}$ electrodes have higher electronic conductivity. The charge/discharge curves of $\text{Si}@\text{C-Ni}$ electrodes at different rates (Fig. 6g) also show that the electrode capacity decays slowly and has better rapid charge/discharge capabilities. The charge/discharge cycle curves of the battery basically agree with the CV curves, which can show the electrochemical reaction process of the battery more clearly.

All in all, the as prepared core-shell structure $\text{Si}@\text{C}$ material is conducive to limiting the volume expansion of silicon, and with the aiding of nickel, the formation of CNWs and graphene nanosheet are both propitious for electronic transmission, and thereof, the as fabricated $\text{Si}@\text{C-Ni}$ electrode exhibits a high electrochemical performance. Besides, compared with $\text{Si}@\text{C}$ electrode, the $\text{Si}@\text{C-Ni}$ electrode after cycling remains relatively intact with no obvious microcracks, which indicates that the pulverization of the electrode has been optimized (Fig. S4).

4. Models and methodology

4.1. Simulation on Li^+ diffusion by COMSOL Multiphysics

The diffusion of lithium ion in solid particles satisfies the following equation [49,50]:

$$D_{\text{Li}^+} = \frac{r^2}{t} \quad (1)$$

Where: D_{Li^+} is the diffusion coefficient of Li^+ in the electrode solid particles (unit: cm² s⁻¹), and the diffusion coefficient of lithium in silicon is 1×10^{-13} cm² s⁻¹ [51]. r is the solid particle radius of the electrode material (unit: cm), and t is the diffusion time of Li^+ in the electrode solid particles (unit: s).

According to Eq. (1), in order to achieve a full charge with rate of 1 C (4200 mA g⁻¹), the anode silicon particle size should be less than 380 nm.

The two difference structures of micron silicon are sketched in Fig. 7. As indicated in Fig. 7a, it is a micron silicon with granular structure, and Fig. 7b is a micron silicon with lamellar structure. The Li^+ diffusion in these two micron silicon structures can be simulated by COMSOL Multiphysics based on the Fick first law of diffusion, and the results show that within 1.0 C charge rate, the Li^+ distribution in granular micron silicon (in Fig. 7c) is inhomogeneous, and only a thin layer close to the surface achieves full charge, such as the orange layer in Fig. 7a, so a 2D model for surface diffusion is available for molecular dynamic (MD) simulation in this case. On the contrary, as indicated in Fig. 7d, the Li^+ concentration in the lamellar micron silicon is quite uniform, so that a 3D model for bulk diffusion is more appropriate for the Lamellar micron silicon.

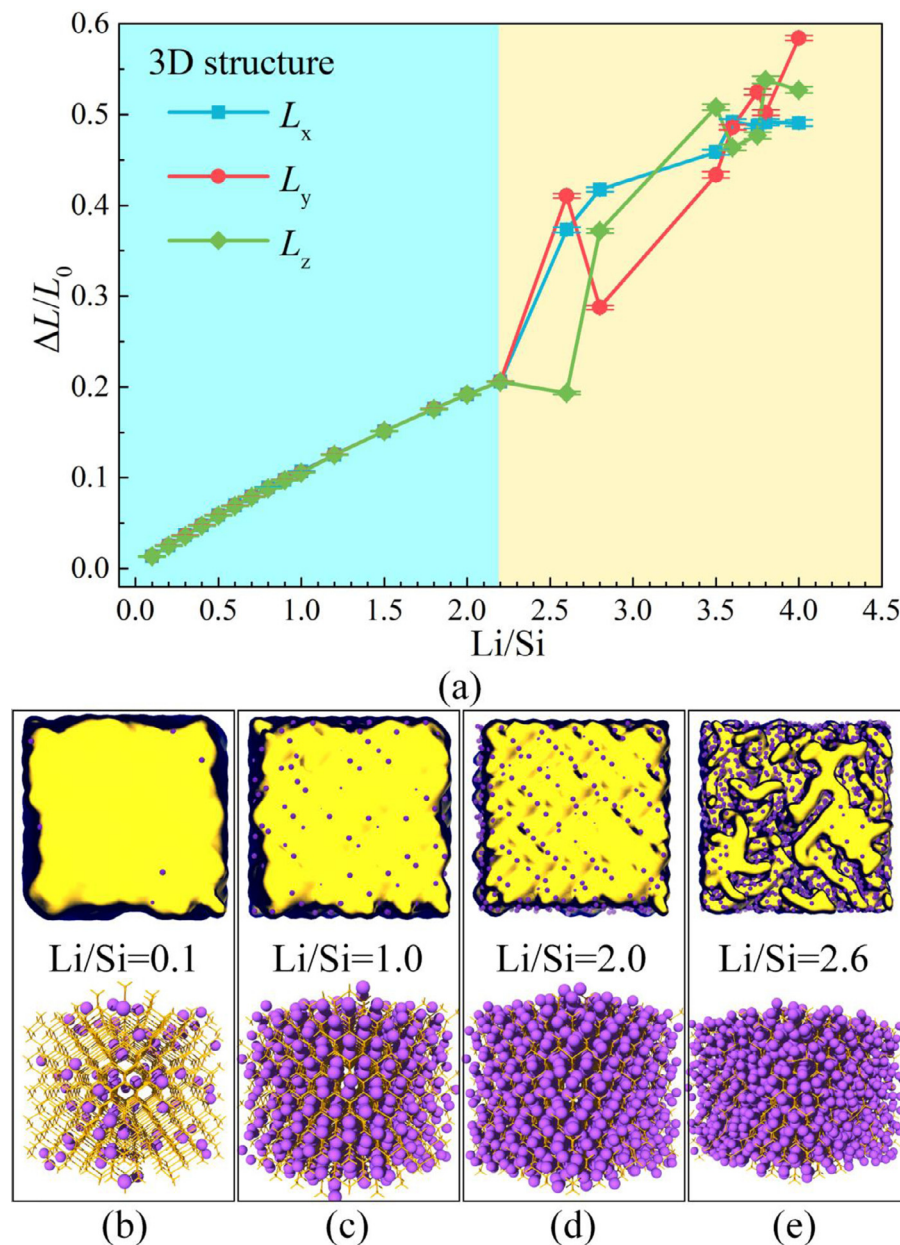


Fig. 8. MD simulation of silicon 3D structure: (a) $\Delta L/L_0$ as a function of Li/Si ratio, and the MD crack view of (b) Li/Si=0.1, (c) Li/Si=1.0, (d) Li/Si=2.0, (e) Li/Si=2.6.

4.2. Molecular Dynamic Simulation

4.2.1. Models

Based on the diffusion simulation, it is clear that the micron silicon with granular structure has a full charge layer, while the lamellar structure obtains a uniform full charge. Therefore, to examine the lithiation-induced volume expansion of silicon, two different models of silicon, including bulky and two-dimensional (2D) silicon, are taken into investigations similar to the experimental samples. But it is worth noting that, for bulky silicon, a cubic structure with dimensions of $27.15 \times 27.15 \times 27.15 \text{ \AA}^3$ is constructed, which coincides with Fig. 7b the lamellar structure. For this model, periodic boundary conditions are applied in all three orthogonal directions. With regard to the 2D silicon, which related to the granular structure of micron silicon in Fig. 7a, a simulated box with dimensions of $94.27 \times 26.60 \times 24.00 \text{ \AA}^3$, in which the thickness of silicon in the x direction is 51.92 \AA . Periodic boundary conditions are applied in the y and z directions to mimic a 2D structure.

4.2.2. Methodology

To simulate the lithiation in both bulky and 2D silicon, Li atoms are initially randomly inserted into silicon samples without physical diffusion process. Then, prior to structural relaxation, Li-inserted silicon are quasi-statically relaxed to a local minimum configuration with an energy and force tolerance of $1.0 \times 10^{-4} \text{ eV}$ and $1.0 \times 10^{-4} \text{ eV \AA}^{-1}$, through the conjugate gradient method, respectively, where the silicon atoms are fixed to maintain silicon framework. Finally, MD runs of 1000000 timesteps are performed to fully relax the Li-inserted silicon at temperature of 300.0 K and confining pressure of 1.0 bar under NPT (constant number of particles, constant pressure, and constant temperature) ensemble. The pressure and temperature are controlled by Nosé-Hoover barostat and thermostat with damping time of 100 timesteps and 1000 timesteps, respectively. A small timestep of 0.1 fs with the velocity-Verlet method is utilized to integrate the Newton's equation of atomic motions in the MD relaxations. The edge lengths of simulated systems are recorded to examine the lithiation-induced volume expansion of silicon.

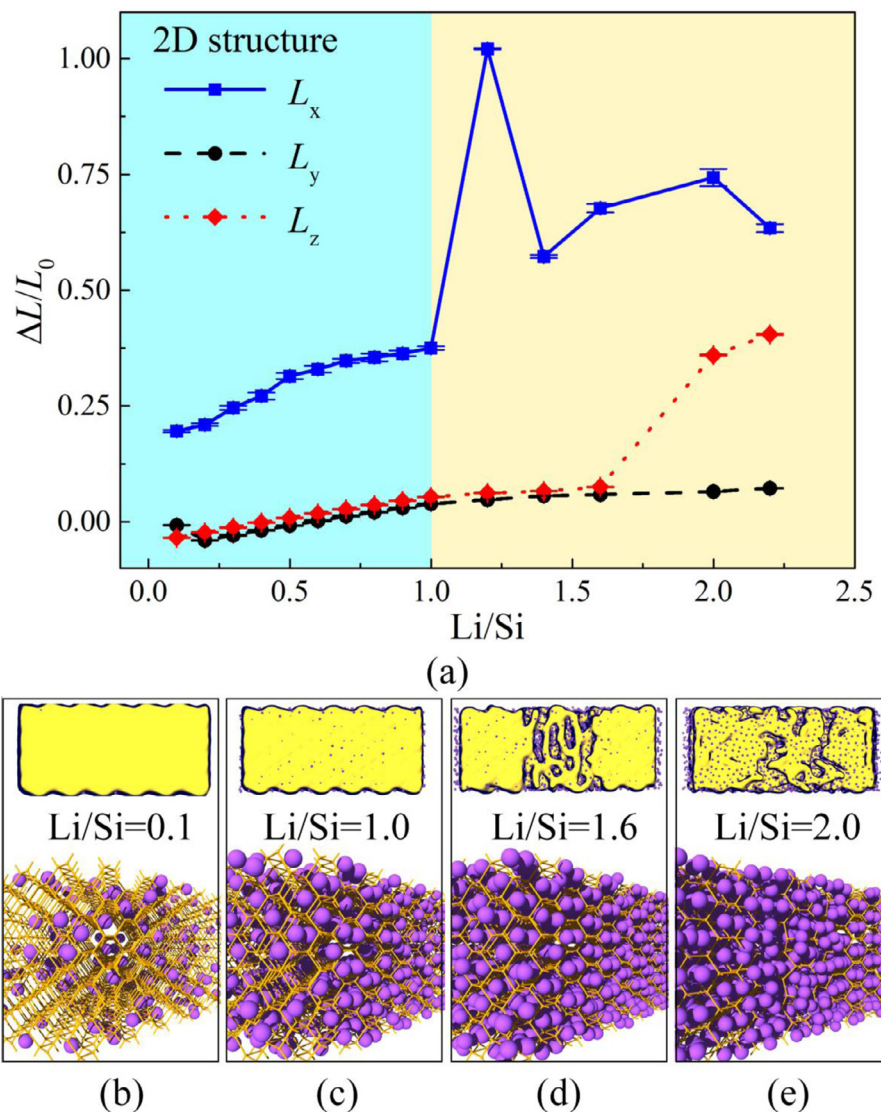


Fig. 9. MD simulation of a silicon 2D structure: (a) $\Delta L/L_0$ as a function of Li/Si ratio, and the MD crack view of (b) Li/Si=0.1, (c) Li/Si=1.0, (d) Li/Si=1.6, (e) Li/Si=2.0.

4.2.3. Forcefield

All MD simulations are performed using the Large-scale Atomic/Molecular Massively Parallel Simulator (LAMMPS) package with a reactive forcefield (ReaxFF) for our Li-inserted silicon systems. ReaxFF is a highly transferable empirical reactive potential based on atomic bond-order/bond distance notion, allowing for describing formation and dissociation of bond during molecular dynamics calculations. ReaxFF has successfully simulated chemical reactions in several systems, such as metals, ceramics, and organic compounds. ReaxFF has been successfully applied to mimic the materials behavior under conditions of straining and temperature [52,53], as well as properties of silicon-based complex battery materials and interfaces [54,55]. In this work, the version of first-principles based ReaxFF developed by Ostadhosseini et al. [54] for Li-Si-based systems is adopted.

4.2.4. Simulation results

The MD simulation results of 3D structure are shown in Fig. 8.

As is shown in Fig. 8a, the volume change keeps a good linear relationship to the Li/Si ratio and there isn't any crack happened in the silicon when the Li/Si ratio is smaller than 2.2 (see Fig. 8b, c, and d), and the crack will occur at the Li/Si ratio larger than 2.6 (see Fig. 8e), which means the lamellar micron silicon can achieve a stable lithium intercalating capacity larger than 2100 mAh g^{-1} , comparing to the $\text{Li}_{4.4}\text{Si}$ (4200 mAh g^{-1}) [56], which agrees well with our experimental results,

here the as prepared Si@C-Ni anode can retain a specific discharge capacity of $2514.8 \text{ mAh g}^{-1}$ after 360 cycles under a current of 0.1 C.

By comparison, the MD simulation of the silicon 2D structure is shown in Fig. 9. The damage Li/Si ratio limits on X, Y, and Z directions are difference, thus as a whole, the damage is decided by the weakest X direction (see Fig. 9a). Therefore, the 2D structure will start its crack at Li/Si ratio of 1.0 (see Fig. 9b, c, d, and e), which suggests that a granular micron silicon is not suitable as anode of LIBs.

5. Conclusion

In this study, using silicon waste from wafer slicing via diamond wire saw technology in photovoltaic industry as raw materials, adding glucose as carbon sources, submicron core-shell Si@C balls intertwined with CNWs and graphene nanosheet, were prepared as anode materials for LIBs by hydrothermal process, where nickel acetate tetrahydrate was added as catalyst. The as prepared Si@C-Ni electrode has an initial specific discharge capacity of $3317.6 \text{ mAh g}^{-1}$ with a coulombic efficiency of 76.76%, and retains a specific discharge capacity of $2514.8 \text{ mAh g}^{-1}$ with capacity retention of 75.8% after 360 cycles under a current of 0.1 C, $1548.9 \text{ mAh g}^{-1}$ after 1000 cycles under 0.2 C. Besides, it maintains 2776.7 , 2291.1 , 2051.7 , 1862.5 , 1630.6 , 1596.9 , 925.3 mAh g^{-1} at each current rate of 0.1 C to 2.0 C, and recovers to a discharge capacity of $\sim 3000 \text{ mAh g}^{-1}$ when the current rate returns to 0.1 C. A COMSOL Mul-

tiphysics simulation is carried out to clarify the Li diffusion in granular and lamellar micron silicon. It determines that the Li^+ concentration in lamellar micron silicon is more homogeneous than that in granular micron silicon. Further, a MD simulation is performed to examine the lithiation-induced volume expansion of silicon. The results demonstrate that, the lamellar micron silicon can achieve a stable lithium intercalating capacity larger than 2100 mAh g^{-1} , which agrees well with our experimental results. It also pointed out that the granular micron silicon is not suitable as anode of LIBs. It is significant in this work, that the lamellar submicron Si, which is from the kerf waste in the photovoltaic slicing process via diamond wire saw technology, is demonstrated to be available as direct raw materials for high performance anode of LIBs.

Data Availability

Data will be made available on request.

Declaration of Competing Interest

The authors declare no conflict of interest.

CRediT authorship contribution statement

Zhengqing Fan: Writing – original draft, Methodology, Conceptualization, Validation, Investigation, Data curation. **Yiting Wang:** Writing – original draft, Methodology, Conceptualization, Validation, Investigation. **Songsheng Zheng:** Project administration, Conceptualization, Writing – review & editing, Supervision, Funding acquisition, Resources. **Ke Xu:** Methodology, Formal analysis. **Jianyang Wu:** Supervision, Resources. **Si Chen:** Investigation. **Junhua Liang:** Investigation. **Aodi Shi:** Investigation. **Zhaolin Wang:** Supervision, Project administration, Funding acquisition.

Acknowledgement

The authors appreciate the supports of the **National Natural Science Foundation of China** (Grant No: 21875199), the National “Double First-class” Construction Special Funds Project (Grant No: 0290-X2100502), the University-Industry-Research Cooperation Project in Fujian Province (Grant No: 2018H6021), and the **Development fund of College of Energy**, Xiamen University (Grant No: 2017NYFZ05).

Supplementary materials

Supplementary material associated with this article can be found, in the online version, at doi:[10.1016/j.ensm.2021.04.005](https://doi.org/10.1016/j.ensm.2021.04.005).

References

- [1] S. Chu, A. Majumdar, *Nature* 488 (2012) 294–303.
- [2] N. Nitta, F. Wu, J.T. Lee, G. Yushin, *Materials Today* 18 (2015) 252–264.
- [3] J. Luo, B. Ma, J. Peng, Z. Wu, Z. Luo, X. Wang, *ACS Sustainable Chemistry & Engineering* 7 (2019) 10415–10424.
- [4] H. Jia, P. Gao, J. Yang, J. Wang, Y. Nuli, Z. Yang, *Advanced Energy Materials* 1 (2011) 1036–1039.
- [5] R.B. Cervera, N. Suzuki, T. Ohnishi, M. Osada, K. Mitsuishi, T. Kambara, K. Takada, *Energy Environ. Sci.* 7 (2014) 662–666.
- [6] Q. Shi, J. Zhou, S. Ullah, X. Yang, K. Tokarska, B. Trzebicka, H.Q. Ta, M.H. Rümmeli, *Energy Storage Materials* 34 (2021) 735–754.
- [7] X. Shen, Z. Tian, R. Fan, L. Shao, D. Zhang, G. Cao, L. Kou, Y. Bai, *Journal of Energy Chemistry* 27 (2018) 1067–1090.
- [8] B. Wang, X. Li, X. Zhang, B. Luo, M. Jin, M. Liang, S.A. Dayeh, S.T. Picraux, L. Zhi, *ACS Nano* 7 (2013) 1437–1445.
- [9] F. Dou, L. Shi, G. Chen, D. Zhang, *Electrochemical Energy Reviews* 2 (2019) 149–198.
- [10] P. Li, H. Kim, S.-T. Myung, Y.-K. Sun, *Energy Storage Materials* 35 (2021) 550–576.
- [11] Y. Jin, B. Zhu, Z. Lu, N. Liu, J. Zhu, *Advanced Energy Materials* 7 (2017).
- [12] U. Kasavajjula, C. Wang, A.J. Appleby, *Journal of Power Sources* 163 (2007) 1003–1039.
- [13] S.W. Lee, M.T. McDowell, J.W. Choi, Y. Cui, *Nano Lett* 11 (2011) 3034–3039.
- [14] X.H. Liu, H. Zheng, L. Zhong, S. Huang, K. Karki, L.Q. Zhang, Y. Liu, A. Kushima, W.T. Liang, J.W. Wang, J.H. Cho, E. Epstein, S.A. Dayeh, S.T. Picraux, T. Zhu, J. Li, J.P. Sullivan, J. Cumings, C. Wang, S.X. Mao, Z.Z. Ye, S. Zhang, J.Y. Huang, *Nano Lett* 11 (2011) 3312–3318.
- [15] J. Gonzalez, K. Sun, M. Huang, J. Lambros, S. Dillon, I. Chasiotis, *Journal of Power Sources* 269 (2014) 334–343.
- [16] K. Eom, T. Joshi, A. Bordes, I. Do, T.F. Fuller, *Journal of Power Sources* (2014) 249.
- [17] Y. Jin, S. Li, A. Kushima, X. Zheng, Y. Sun, J. Xie, J. Sun, W. Xue, G. Zhou, J. Wu, F. Shi, R. Zhang, Z. Zhu, K. So, Y. Cui, J. Li, *Energy & Environmental Science* 10 (2017) 580–592.
- [18] T. Song, H. Cheng, H. Choi, J.-H. Lee, H. Han, D.H. Lee, D.S. Yoo, M.-S. Kwon, J.-M. Choi, S.G. Doo, H. Chang, J. Xiao, Y. Huang, W.I. Park, Y.-C. Chung, H. Kim, J.A. Rogers, U. Paik, *ACS Nano* 6 (2012) 303–309.
- [19] T. Wada, T. Ichitsubo, K. Yubuta, H. Segawa, H. Yoshida, H. Kato, *Nano Lett* 14 (2014) 4505–4510.
- [20] M.-H. Park, M.G. Kim, J. Joo, K. Kim, J. Kim, S. Ahn, Y. Cui, J. Cho, *Nano Lett* 9 (2009) 3844–3847.
- [21] J. Kaspar, M. Graczyk-Zajac, S. Lauterbach, H.-J. Kleebe, R. Riedel, *Journal of Power Sources* 269 (2014) 164–172.
- [22] M. Furquan, A. Raj Khatribail, S. Vijayalakshmi, S. Mitra, *Journal of Power Sources* 382 (2018) 56–68.
- [23] R.-C. Chen, L.-Y. Hsiao, C.-Y. Wu, J.-G. Duh, *Journal of Alloys and Compounds* 791 (2019) 19–29.
- [24] H. Chen, Z. Wang, X. Hou, L. Fu, S. Wang, X. Hu, H. Qin, Y. Wu, Q. Ru, X. Liu, S. Hu, *Electrochimica Acta* 249 (2017) 113–121.
- [25] L. Gan, H. Guo, Z. Wang, X. Li, W. Peng, J. Wang, S. Huang, M. Su, *Electrochimica Acta* 104 (2013) 117–123.
- [26] T. Zhao, S. She, X. Ji, W. Jin, A. Dang, H. Li, T. Li, S. Shang, Z. Zhou, *Journal of Alloys and Compounds* 708 (2017) 500–507.
- [27] Y. Fan, Q. Zhang, Q. Xiao, X. Wang, K. Huang, *Carbon* 59 (2013) 264–269.
- [28] J. Ryu, T. Bok, S.H. Joo, S. Yoo, G. Song, S.H. Kim, S. Choi, H.Y. Jeong, M.G. Kim, S.J. Kang, C. Wang, S.K. Kwak, S. Park, *Energy Storage Materials* 36 (2021) 139–146.
- [29] B. Jiang, S. Zeng, H. Wang, D. Liu, J. Qian, Y. Cao, H. Yang, X. Ai, *ACS Appl Mater Interfaces* 8 (2016) 31611–31616.
- [30] X. Yu, P. Wang, X. Li, D. Yang, *Solar Energy Materials and Solar Cells* 98 (2012) 337–342.
- [31] N. Drouiche, P. Cuellar, F. Kerkar, S. Medjahed, N. Boutouchent-Guerfi, M. Ould Hamou, *Renewable and Sustainable Energy Reviews* 32 (2014) 936–943.
- [32] Q. Bao, Y.-H. Huang, C.-K. Lan, B.-H. Chen, J.-G. Duh, *Electrochimica Acta* 173 (2015) 82–90.
- [33] C.-C. Hsieh, W.-R. Liu, *Journal of Alloys and Compounds* 790 (2019) 829–836.
- [34] H.-G. Tan, J.-G. Duh, *Journal of Power Sources* 335 (2016) 146–154.
- [35] N.P. Wagner, A. Tron, J.R. Tolchard, G. Noia, M.P. Bellmann, *Journal of Power Sources* 414 (2019) 486–494.
- [36] S.K. Kim, H. Kim, H. Chang, B.G. Cho, J.X. Huang, H. Yoo, H. Kim, H.D. Jang, *Scientific Reports* 6 (2016) 8.
- [37] Z. Fan, S. Zheng, S. He, Y. Ye, J. Liang, A. Shi, Z. Wang, Z. Zheng, *Diamond and Related Materials* 107 (2020) 107898.
- [38] A.C. Ferrari, J.C. Meyer, V. Scardaci, C. Casiraghi, M. Lazzeri, F. Mauri, S. Pisacane, D. Jiang, K.S. Novoselov, S. Roth, A.K. Geim, *Phys Rev Lett* 97 (2006) 187401.
- [39] P. Pachfule, D. Shinde, M. Majumder, Q. Xu, *Nat Chem* 8 (2016) 718–724.
- [40] J. Riikonen, W. Kim, C. Li, O. Svensk, S. Arpiainen, M. Kainlauri, H. Lipsanen, *Carbon* 62 (2013) 43–50.
- [41] L.M. Malard, M.A. Pimenta, G. Dresselhaus, M.S. Dresselhaus, *Physics Reports* 473 (2009) 51–87.
- [42] M. Zheng, K. Takei, B. Hsia, H. Fang, X. Zhang, N. Ferralis, H. Ko, Y.-L. Chueh, Y. Zhang, R. Maboudian, A. Javey, *Applied Physics Letters* 96 (2010) 063110.
- [43] R. Wenisch, R. Hübner, F. Munnik, S. Melkhanova, S. Gemming, G. Abrasonis, M. Krause, *Carbon* 100 (2016) 656–663.
- [44] K.-H. Liao, J.-M. Ting, *Carbon* 42 (2004) 509–514.
- [45] H. Murata, N. Saitoh, N. Yoshizawa, T. Suemasu, K. Toko, *Applied Physics Letters* 111 (2017) 243104.
- [46] H. Li, X. Li, J. Wei, Z. Wang, P. Guo, P. Ke, H. Saito, P. Cui, A. Wang, *Diamond and Related Materials* 101 (2020).
- [47] S. Guo, H. Li, H. Bai, Z. Tao, J. Chen, *Journal of Power Sources* 248 (2014) 1141–1148.
- [48] Y.Q. Zhang, X.H. Xia, X.L. Wang, Y.J. Mai, S.J. Shi, Y.Y. Tang, C.G. Gu, J.P. Tu, *Journal of Power Sources* 213 (2012) 106–111.
- [49] K.M. Abraham, *J Phys Chem Lett* 6 (2015) 830–844.
- [50] P.G. Bruce, B. Scrosati, J.M. Tarascon, *Angew Chem Int Ed Engl* 47 (2008) 2930–2946.
- [51] T.L. Kulova, A.M. Skundin, Y.V. Pleskov, E.I. Terukov, O.I. Kon'kov, *Journal of Electroanalytical Chemistry* 600 (2007) 217–225.
- [52] H. Zhao, Q. Shi, Z. Han, H. Gong, Z. Zhang, S. Wu, J. Wu, *Carbon* 138 (2018) 243–256.
- [53] C. Sui, Y. Zhao, Z. Zhang, J. He, Z. Zhang, X. He, C. Wang, J. Wu, *ACS Omega* 2 (2017) 3977–3988.
- [54] A. Ostadhosseini, S.Y. Kim, E.D. Cubuk, Y. Qi, A.C. van Duin, *J Phys Chem A* 120 (2016) 2114–2127.
- [55] K.S. Yun, S.J. Pai, B.C. Yeo, K.R. Lee, S.J. Kim, S.S. Han, *J Phys Chem Lett* 8 (2017) 2812–2818.
- [56] B.A. Boukamp, G.C. Lesh, R.A. Huggins, *Journal of the Electrochemical Society* 128 (1981) 725–728.